ORIGINAL PAPER

An efficient phase-field model of shear fractures using deviatoric stress split

Ehsan Haghighat[1] · David Santillán[2]

Abstract

We propose a phase-field model of shear fractures using the deviatoric stress decomposition. This choice allows us to use general three-dimensional Mohr–Coulomb's failure function for formulating the relations and evaluating peak and residual stresses. We apply the model to a few benchmark problems of shear fracture and strain localization and report remarkable performance. Our model is able to capture *conjugate* failure modes under biaxial compression test and for the slope stability problem, a challenging task for most models of geomechanics.

Keywords Phase-field · Shear fracture · Strain localization · Slope stability

1 Introduction

The shear failure of brittle materials in compression, also known as shear bands or localized strains, are one of the dominant modes of failure in geo-structures. It has recently emerged as an active research topic due to its interest in structural geology and engineering. The growing interest stems from its engineering applications in subsurface energy technologies, including enhanced geothermal energy systems where the hydro-shearing technique is aimed to reactivate and slide the preexisting fracture network to increase the rock mass permeability [1–4], large-scale CO_2 sequestration in deep saline aquifers [5–7], impoundment and level changes of artificial water reservoirs of hydropower plants [8–11] and underground natural gas storage facilities [12], where their mechanics are crucial to understanding the stability of faults and hence earthquake mechanisms [13–16]. Other engineering applications include fault and slope stability assessment [17, 18], or the stability of faults during the groundwater injection and production operations [19, 20].

The simulation of shear fracturing processes is a challenging task. The finite element method (FEM) has been the dominant numerical method for modeling solids and continua. Classically, two fundamentally different perspectives are proposed to study compressive fractures using FEM:

– Discrete fracture models (DFM) that are based on the classical theory of linear elastic fracture mechanics (LEFM) founded by Griffith [21] and Irwin [22].
– Smeared fracture models (SFM) that are based on the classical theory of continuum damage mechanics (CDM) proposed initially by Kachanov [23].

Each class includes extensive literature dating back to the 1960s that is out of the scope of this text to cover comprehensively. Therefore we only point the interested reader to a few primary studies of each class.

Within the DFM realm, common approaches include node duplication on fracture interface [24–26], strong discontinuity approaches [27–38], and extended finite element methods (XFEM) [36, 39–47]. These methods require using geometrical algorithms to trace the fracture propagation, which has been found very challenging for generic three-dimensional setups. Such methods are efficient for modeling single fractures. However, they become quickly impractical when dealing with complex fracture nucleation and propagation patterns.

As per the SFMs, we can point to continuum damage models (CDM) [23, 26, 48–52], peridynamic models [53–62], and

✉ David Santillán
david.santillan@upm.es

1 Department of Civil and Environmental Engineering, Massachusetts Institute of Technology, 77 Massachusetts Ave, Cambridge 02139, MA, USA

2 Departamento de Ingenería Civil: Hidráulica, Energía y Medio Ambiente, Universidad Politécnica de Madrid, C/Profesor Aranguren 3, 28040 Madrid, Spain

phase-field models (PFM) [63–68], which we discuss next in more details. While early models showed significant mesh dependencies, these models have been used to simulate very complex fracture patterns under realistic conditions. Among this class, phase-field models have been most attractive in recent years due to their thermodynamically sound foundations and their ability to model complex fracture patterns.

Phase-field models have been extensively used for modeling brittle, cohesive, and ductile Mode-I fracture patterns, in elastic or poroelastic materials and homogeneous or heterogeneous domains [63–78] [see [79], for a detailed review]. Although Lancioni and Royer-Carfagni [98] proposed a simple extension for shear fractures, the applicability of phase-field for modeling shear failure remained virtually untouched until very recently [80–82]. In a detailed study, Fei and Choo [82] presented a phase-field formulation of frictional fracture based on Palmer and Rice [83] theory and using a similar stress decomposition approach to the one proposed by Hu et al. [89] for tensile cracks. The authors validated their model on a set of classical problems as well as various experimental setups [84].

In the present study, we propose a phase field model of shear failure that adapts the cohesive model of shear fractures proposed by Fei and Choo [82] for deviatoric stress decomposition (DSD) instead of the proposed contact stress decomposition (CSD). Hence, we arrive at an alternative descriptor for the shear fracture orientation (i.e., the $\boldsymbol{\alpha}$ tensor) which is solely based on the deviatoric strain. We adapt the crack driving force to be consistent with the DSD decomposition. The resulting formulation simplifies the damage criterion since it results in damaging the shear modulus. Lastly, the proposed model allows us to use the general forms of the failure functions from the classical plasticity theory and therefore is not limited to Mohr–Coulomb failure model.

In what follows, we first briefly describe the original framework based on CSD. We then discuss our generalization proposal. Lastly, we use both frameworks to model a set of benchmark problems.

2 Phase-field method

In this section, we first describe the general phase-field framework for modeling crack propagation in materials. We then summarize the most recent CSD shear model [82]. Finally, we discuss our proposed adjustment for better stability.

2.1 Phase-field governing equations

Consider the continua $\Omega \in \mathbb{R}^D$ in D-dimensional space, depicted in Fig. 1, with its boundary represented as Γ. The boundary Γ is subjected to Neumann boundary conditions on Γ_t and Dirichlet boundary conditions on Γ_u, where $\Gamma_u \cup \Gamma_t =$

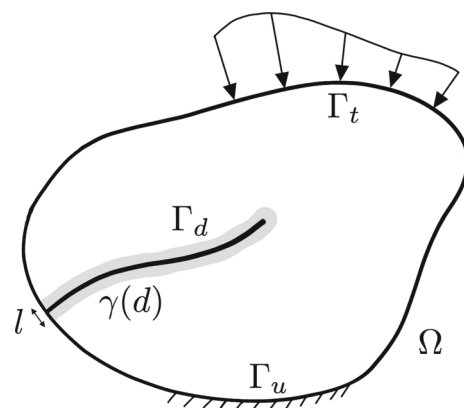**Fig. 1** Domain Ω with boundary Γ, Dirichlet boundary Γ_u, and Neumann boundary Γ_t. The discontinuity surface is represented by Γ_d with its phase-field diffused representation as $\gamma(d)$

Γ and $\Gamma_u \cap \Gamma_t = \varnothing$. The set of discontinuities in the domain is represented by a discrete surface Γ_d. The crack's intersection with the boundary is considered a Neumann-type boundary condition.

According to the phase-field formulation, the fracture's discrete surface Γ_d is approximated implicitly as a continuous function over a width l using the Allen–Cahn fracture surface density function $\gamma(d)$ as

$$\gamma(d) = \frac{1}{c_0 l}\left(w(d) + l^2 \|\nabla d\|^2\right), \text{ with } c_0 = 4\int_0^1 \sqrt{w(l)}dl \tag{1}$$

where d is the phase-field variable, with $d = 0$ presenting the intact part of the domain while $d = 1$ expressing a point on Γ_d. $w(d)$ is the transition function, also known as the dissipation function, defined for cohesive cracks as $w(d) = d$ [85, 86], hence $c_0 = \frac{8}{3}$. Accordingly, a surface integral $\int ds$ is approximated using a volume integral as $\int ds \approx \int \gamma(d) \, dv$.

Assuming small deformation kinematics, and given the displacement field $\boldsymbol{u}$, the strain field is expressed by $\boldsymbol{\varepsilon} = (\nabla \boldsymbol{u} + \nabla \boldsymbol{u}^T)/2$, and the crack surface density function $\gamma(d)$, the total energy of a fractured continua, occupying the domain Ω and bounded by the boundary Γ, shown in Fig. 1, is expressed as

$$\Psi = -\Psi^{external} + \Psi^{internal} + \Psi^{fracture}, \tag{2}$$

where $\Psi^{external}$ is the work done by the external traction stress $\boldsymbol{\tau}$ and body force $\boldsymbol{b}$, and expressed as

$$\Psi^{external} = \int_{\Gamma_t} \boldsymbol{u} \cdot \boldsymbol{\tau} \, ds + \int_\Omega \boldsymbol{u} \cdot \boldsymbol{b} \, dv. \tag{3}$$

The fracture energy, i.e., $\Psi^{fracture}$, is the energy dissipated from the system to create a fracture surface Γ_d. Given the energy release rate $\mathcal{G}_c$ (per unit fracture length), $\Psi^{fracture}$ is expressed as

$$\Psi^{fracture} = \int_{\Gamma_d} \mathcal{G}_c \, ds \approx \int_{\Omega} \mathcal{G}_c \gamma(d) \, dv. \tag{4}$$

The stored internal energy of the system $\Psi^{internal}$ consists of the elastic stored energy in the intact part of the domain and stored energy in the damaged part of the domain, expressed as

$$\Psi^{internal} = \int_{\Omega} \psi(\boldsymbol{\varepsilon}, d) \, dv. \tag{5}$$

The internal energy density function $\psi(\boldsymbol{\varepsilon}, d)$ is defined as $\psi(\boldsymbol{\varepsilon}, d) = \frac{1}{2}\boldsymbol{\sigma} : \boldsymbol{\varepsilon}$, which consists of both inactive and damaged counterparts. For the intact part of continuum, i.e., where $d = 0$, the Cauchy stress tensor $\boldsymbol{\sigma}(\boldsymbol{\varepsilon}, d = 0)$ is expressed using Hook's law as

$$\boldsymbol{\sigma}(\boldsymbol{\varepsilon}, d = 0) = \left(\kappa - \frac{2}{3}\mu\right)\varepsilon_v \mathbf{1} + 2\mu\boldsymbol{\varepsilon}, \tag{6}$$

where κ and μ are bulk and shear moduli of the intact material, respectively, and ε_v is the volumetric strain, expressed as $\varepsilon_v = \text{tr}(\boldsymbol{\varepsilon})$. For the parts of the domain where $d > 0$, the Cauchy stress tensor is decomposed into inactive part $\boldsymbol{\sigma}^I$ and active part $\boldsymbol{\sigma}^A$ as

$$\begin{aligned} \boldsymbol{\sigma}(\boldsymbol{\varepsilon}, d) &= \boldsymbol{\sigma}^I(\boldsymbol{\varepsilon}) + \boldsymbol{\sigma}^A(\boldsymbol{\varepsilon}, d) \\ &= \boldsymbol{\sigma}^I(\boldsymbol{\varepsilon}) + g(d)\hat{\boldsymbol{\sigma}}(\boldsymbol{\varepsilon}) + (1 - g(d))\tilde{\boldsymbol{\sigma}}(\boldsymbol{\varepsilon}). \end{aligned} \tag{7}$$

The active part of the stress tensor undergoes the damage process, and $g(d)$ is a degradation function that expresses the stress transition from bulk ($\hat{\boldsymbol{\sigma}}$) to fracture ($\tilde{\boldsymbol{\sigma}}$). We will discuss these in more details in the next sections.

Therefore, there are two solution variables associated with the phase-field formulation, the standard displacement field $\boldsymbol{u}$ and the additional phase-field variable d. Taking the variation of Ψ with respect to $\boldsymbol{u}$ and d, and following the standard *weak to strong* form steps of the FEM [87, 88] and phase-field [73, 82, 89], we can arrive at the following governing relations:

$$\nabla \cdot \boldsymbol{\sigma}(\boldsymbol{\varepsilon}, d) + \boldsymbol{b} = 0, \tag{8}$$

$$\frac{3\mathcal{G}_c}{8l}\left(2l^2\nabla^2 d - 1\right) - g'(d)\mathcal{H}(\boldsymbol{\varepsilon}) = 0. \tag{9}$$

The irreversibility of the fracture process is guaranteed with the local history field of maximum stored shear energy $\mathcal{H}^+(\boldsymbol{\varepsilon})$ that allows us to solve the constrained minimization of Eq.(9) in a straightforward way [67] and avoids unphysical self-healing. $\mathcal{H}^+(\boldsymbol{\varepsilon})$ is defined as follows:

$$\mathcal{H}^+(\boldsymbol{\varepsilon}) = \max_{s \in [0,t]} \left(\mathcal{H}(\boldsymbol{\varepsilon})\right), \tag{10}$$

where t is time. Equation (9) is then rewritten as follows:

$$\frac{3\mathcal{G}_c}{8l}\left(2l^2\nabla^2 d - 1\right) - g'(d)\mathcal{H}^+(\boldsymbol{\varepsilon}) = 0. \tag{11}$$

Since $\dot{\mathcal{H}} \geq 0$, non-negative $\dot{d}$ is guaranteed and, consequently, the irreversibility of the fracture growth. We define $\mathcal{H}(\boldsymbol{\varepsilon})$ after describing the stress decomposition approach.

In this work, we use the Lorenz degradation function $g(d)$ defined as [90, 91]:

$$g(d, \mathfrak{p}) = \frac{(1 - d)^2}{(1 - d)^2 + \frac{M}{\psi_c}d(1 + \mathfrak{p}d)} \tag{12}$$

where, $M = G_c/(c_0 l)$ and ψ_c is the critical crack driving force at the material's peak strength, evaluated as $\psi_c = -Mw'(0)/g'(0)$. The damage begins to accumulate as soon as elastic stored energy exceeds this critical threshold. Here, we take $\mathfrak{p} = 1$.

2.2 Stress decomposition: introduction

The split of the strain energy density into crack driving and intact components defines the damage mode and fracture pattern. Up to date, two fundamental approaches are available. The approaches of the first class do not take into account the local fracture orientation, whereas the second approaches take into consideration the local crack orientation.

The first group of models includes the isotropic model, the volumetric and deviatoric decomposition model, the spectral decomposition model, or the anisotropic models. The isotropic model proposed by Bourdin et al. [64] where the entire strain energy density is degraded. The volumetric and deviatoric decomposition model proposed by Amor et al. [92] splits the strain tensor into its volumetric and deviatoric components. This approach avoids crack inter-penetration in composites and masonry structures. The fracture is then assumed to be driven by volumetric expansion and deviatoric strains. The spectral decomposition model proposed by Miehe et al. [67] splits the strain tensor into its principal components and only tensile components drive the fracture propagation. The anisotropic models are based on the spectral decomposition of the strain tensor using other projections, such as the eigenvalue and eigenvector of the effective stress tensor [93].

The second group of approaches take into consideration the local crack orientation. The directional model proposed by Steinke and Kaliske [94] splits the stress tensor into the crack driving and persistent components using the fracture orientation. For each point, a fracture coordinate system is defined and the fracture orientation is obtained from the maximum principal stress direction. Strobl and Seelig [95] and Strobl and Seelig [96] computed the fracture orientation from the phase-field gradients. Following this way to compute the fracture direction, Liu et al. [97] developed a phase field

model based on micromechanical modeling, i.e., the macroscopic fracture is modeled as a collection of microscopic fractures.

In the following subsections, we describe the contact stress decomposition (CSD), used satisfactorily to simulate shear fractures under confining pressures, and lastly we present our proposal based on the deviatoric stress decomposition (DSD). Both models do not take into account the local fracture orientation.

2.2.1 Contact stress decomposition (CSD)

Since a compressive fracture behaves like a contact problem, Fei and Choo [82] proposed a stress decomposition approach that is closely related to the contact formulation, which we refer here as CSD. It starts by considering a corotational coordinate system on the fracture surface with m and n as tangential and normal vectors to the crack surface, and m along the direction of sliding. Additionally, let us define $\alpha = (mn + nm)/2$.

According to this approach and under the assumption that the fracture remains closed, i.e., no tensile fracture, the only stress component that should undergo damage is the shear stress, and other stress components remain inactive. The bulk shear stress can be expressed as

$$\hat{\tau} = \hat{\sigma} : \alpha = \mu\varepsilon_\gamma, \tag{13}$$

where $\varepsilon_\gamma = 2\,\varepsilon : \alpha = 2\,m \cdot \varepsilon \cdot n$. Consider the contact shear stress as $\tilde{\tau}$. Then, the inactive stress tensor is expressed as

$$\sigma^I = \sigma(\varepsilon, d = 0) - \mu\varepsilon_\gamma\,\alpha, \tag{14}$$

and the active stress tensor as

$$\sigma^A = \tau^A\alpha, \quad \text{where} \quad \tau^A = \mu\varepsilon_\gamma\,g(d) + \tilde{\tau}\,(1 - g(d)). \tag{15}$$

Here, $\tilde{\tau}$ is the residual contact stress while the fracture is fully developed, i.e., d = 1.

Remark 1 Given the Mohr–Coulomb's failure function as,

$$\mathcal{F} = |\tau| - \sigma_n \tan\phi - c = 0 \tag{16}$$

with $\sigma_n = n \cdot \sigma \cdot n$ as to normal stress on the fracture surface, and c and ϕ as cohesion and friction angle of the intact material, the peak and residual shear stresses are expressed as

$$\tilde{\tau}_p = c + \sigma_n \tan(\phi), \quad \tilde{\tau}_r = c_r + \sigma_n \tan(\phi_r), \tag{17}$$

where c_r and ϕ_r are residual friction and cohesion at the fully developed failure state.

Remark 2 Based on the Mohr–Coulomb failure criterion, the critical plane for the failure is evaluated at two conjugate angles $\theta = \pm(45° - \phi_r/2)$ [27] with respect to the direction of the maximum principal stress. However, the authors only consider $\theta = +(45° - \phi_r/2)$ [see [82], Eq. 56]. This restriction is required otherwise m, n is not uniquely defined.

2.2.2 Our proposal: deviatoric stress decomposition (DSD)

The total strain tensor can be decomposed into volumetric and deviatoric parts, as $\varepsilon = \varepsilon_v\mathbf{1} + e$. We can also express the Cauchy tensor in terms of the mean confining stress p and the deviatoric stress tensor s as $\sigma = -p\mathbf{1} + s$. Therefore, we can re-write Hook's law for the intact part as [98, 99]

$$\sigma(\varepsilon, d = 0) = -p\mathbf{1} + s = \kappa\,\varepsilon_v\mathbf{1} + 2\mu e. \tag{18}$$

Given the equivalent deviatoric (Mises) stress $q = (\frac{3}{2}s : s)^{1/2}$ and the equivalent deviatoric strain $\varepsilon_q = (\frac{2}{3}e : e)^{1/2}$ and with some algebra, we can write that

$$q = 3\mu\varepsilon_q. \tag{19}$$

Let us now define the *Unit Deviator Tensor* α_q as

$$\alpha_q = \sqrt{\frac{2}{3}}\frac{e}{\varepsilon_q}, \quad \text{where} \quad \|\alpha_q\| = \sqrt{\alpha_q : \alpha_q} = 1, \tag{20}$$

Hook's law can therefore be expressed as

$$\sigma = -p\mathbf{1} + \sqrt{\frac{2}{3}}q\alpha_q, \quad \text{where} \quad p = \kappa\varepsilon_v, \quad q = 3\mu\varepsilon_q. \tag{21}$$

Equivalent to the CSD, we can describe the compressive failure in a material as damage in the deviatoric stress component. Therefore, the compressive pressure becomes the inactive part of the stress tensor, i.e.,

$$\sigma^I = -p\mathbf{1} = \kappa\varepsilon_v\mathbf{1}, \tag{22}$$

and active stress is described as

$$\sigma^A = q(\varepsilon, d)\alpha_q, \quad \text{where} \quad q(\varepsilon, d) = g(d)\hat{q} + (1 - g(d))\tilde{q}_r, \tag{23}$$

where the bulk deviatoric stress is $\hat{q} = 3\mu\varepsilon_q$.

Remark 3 This deviatoric stress decomposition allows us to leverage the general form of virtually any failure surface that are described in the classical plasticity theory, including the Mohr–Coulomb failure function. Given the friction angle ϕ

and cohesion coefficient c, the general form of the Mohr–Coulomb's failure criterion is expressed as

$$\mathcal{F} = \mathcal{R}_{MC} q - p \tan \phi - c = 0. \tag{24}$$

Here, $\mathcal{R}_{MC}$ defines the shape of the Mohr–Coulomb's failure surface and is expressed as

$$\mathcal{R}_{MC} = \frac{1}{\sqrt{3} \cos \phi} \sin \left(\Theta + \frac{\pi}{3} \right) + \frac{1}{3} \cos \left(\Theta + \frac{\pi}{3} \right) \tan \phi, \tag{25}$$

where Θ is the Lodè angle, evaluated as $\cos(3\Theta) = (r/q)^3$. The invariant r is the third invariant of the deviatoric stress tensor, and is defined as $r = (\frac{9}{2} tr(\boldsymbol{s}^3))^{1/3}$. Based on this criterion, we can find the peak and residual Mises stresses as

$$\tilde{q}_p = \frac{p \tan \phi + c}{\mathcal{R}_{MC}}, \quad \tilde{q}_r = \frac{p \tan \phi_r + c_r}{\mathcal{R}_{MC}}, \tag{26}$$

with ϕ_r and c_r as the residual values for friction angle and cohesion at the fully damaged state.

Remark 4 We can easily replace the non-smooth Mohr–Coulomb surface $\mathcal{R}_{MC}$ with some alternatives [100, 101]. In fact, we can potentially pick any alternative failure function available for different materials.

2.3 Crack driving force

Given $\tau = \mu \varepsilon_\gamma$ and $\tau_p = p \tan \phi + c = \mu \varepsilon_\gamma^p$, the crack driving force relations for CSD is derived as [82]

$$\mathcal{H} = \mathcal{H}_t + \mathcal{H}_{slip} \tag{27}$$

where

$$\mathcal{H}_t = \frac{\tilde{\tau}_p - \tilde{\tau}_r}{2\mu}, \tag{28}$$

$$\mathcal{H}_{slip} = \frac{1}{2\mu} \left[(\hat{\tau} - \tilde{\tau}_r)^2 - (\tilde{\tau}_p - \tilde{\tau}_r)^2 \right] \tag{29}$$

and they showed that this model is consistent with Palmer and Rice [83] model. Now, for the deviatoric stress decomposition discussed above, we can revise the crack driving force, given $\hat{q} = 3\mu \varepsilon_q$ and $\tilde{q}_p = (p \tan \phi + c)/\mathcal{R}_{MC} = 3\mu \varepsilon_q^p$, as

$$\mathcal{H}_t = \frac{(\tilde{q}_p - \tilde{q}_r)^2}{6\mu}, \tag{30}$$

$$\mathcal{H}_{slip} = \frac{1}{6\mu} \left[(\hat{q} - \tilde{q}_r)^2 - (\tilde{q}_p - \tilde{q}_r)^2 \right]. \tag{31}$$

More details on the derivation of $\mathcal{H}_t$ and $\mathcal{H}_{slip}$ for CSD approach are provided in "Appendix A".

2.4 Boundary conditions

To have a complete mathematical description of the problem, we lastly need to describe the boundary conditions. Considering Fig. 1, the boundary conditions are described as

$$\boldsymbol{u} = \bar{\boldsymbol{u}}, \quad \text{on} \quad \Gamma_u, \tag{32}$$

$$\boldsymbol{\tau} = \boldsymbol{\sigma} \cdot \boldsymbol{n} = \bar{\boldsymbol{\tau}}, \quad \text{on} \quad \Gamma_t, \tag{33}$$

$$\nabla d \cdot \boldsymbol{n} = 0, \quad \text{on} \quad \Gamma, \tag{34}$$

where $\bar{\boldsymbol{u}}$ and $\bar{\boldsymbol{\tau}}$ are prescribed displacement and traction forces, respectively.

The steps used to solve the problem are detailed in Algorithm 1.

Algorithm 1 Pseudo-code for DSS phase-field model of shear fractures

---

1: $\boldsymbol{u}^0, d^0 \leftarrow 0$
2: $\boldsymbol{\sigma}^0 \leftarrow$ Initial stress using an static step
3: $t = 0$
4: **for** time-steps **do**
5:     $t \leftarrow t + \Delta t$
6:     $\bar{\boldsymbol{u}}^{t+\Delta t}, \bar{\boldsymbol{\tau}}^{t+\Delta t} \leftarrow$ Update displacement/traction BCs at $t + \Delta t$
7:     $\boldsymbol{u}_0, \boldsymbol{\varepsilon}_0, \boldsymbol{\sigma}_0, d_0 \leftarrow \boldsymbol{u}_0^t, \boldsymbol{\varepsilon}_0^t, \boldsymbol{\sigma}_0^t, d_0^t$
8:     **while** err > TOL **do**
9:         $\delta \boldsymbol{u} \leftarrow$ Solve eq. (8) for displacement increment
10:        $\boldsymbol{u} \leftarrow \boldsymbol{u} + \delta \boldsymbol{u}$
11:        $\boldsymbol{\varepsilon}, \varepsilon_v, \varepsilon_q \leftarrow \boldsymbol{\varepsilon} + \delta \boldsymbol{\varepsilon}$
12:        $\boldsymbol{\alpha}_q \leftarrow \sqrt{2/3} \, \boldsymbol{e}/\varepsilon$
13:        $\hat{q} \leftarrow 3\mu \varepsilon_q$
14:        $\tilde{q} \leftarrow (p \tan \phi_r + c_r)/\mathcal{R}_{MC}$
15:        $\boldsymbol{\sigma} \leftarrow -\kappa \varepsilon_v \mathbf{1} + \left[g(d)\hat{q} + (1 - g(d))\tilde{q}_r \right] \sqrt{2/3} \boldsymbol{\alpha}_q$
16:        $\mathcal{H}_t \leftarrow (\tilde{q}_p - \tilde{q}_r)^2/6\mu$
17:        $\mathcal{H}_{slip} \leftarrow \max(\mathcal{H}_{slip}^t, \; \left[(\hat{q} - \tilde{q}_r)^2 - (\tilde{q}_p - \tilde{q}_r)^2 \right]/6\mu)$
18:        $\mathcal{H}^+ \leftarrow \mathcal{H}_t + \mathcal{H}_{slip}$
19:        $\delta d \leftarrow$ Solve eq. (9) for d
20:   **end while**
21: **end for**

---

3 Applications to compressive strain localization

Here, we consider three reference problems of shear fractures, including direct shear test, biaxial compression test, and slope failure analysis. We show that our model can effectively capture multiple modes of failure concurrently.

3.1 Direct shear test

Our first example is the direct shear test. We simulate the propagation of a fracture in a long shear apparatus and we compare our results with analytical solutions and Fei and

Fig. 2 Direct shear test setup. The domain is 500 mm long, 100 mm tall, and an initial 10-mm horizontal fracture is carved in the middle of the left boundary—red fracture. The boundary conditions are: the bottom boundary is fixed, the top boundary is displaced horizontally, and the two lateral boundaries are fixed vertically
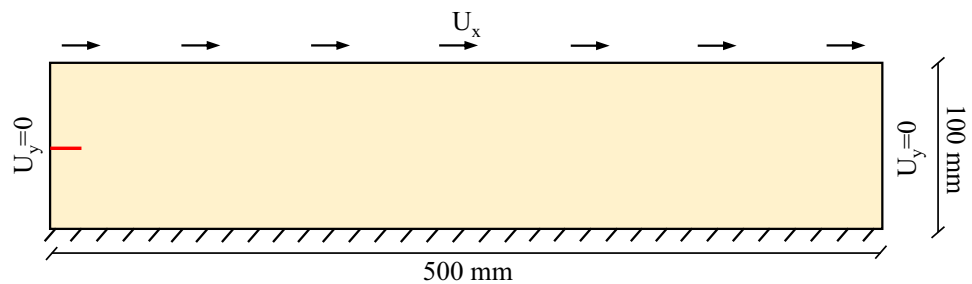
Choo's numerical simulations [82]. The setup of the experiment is plotted in Fig. 2. The domain is 500 mm long, 100 mm tall, and an initial 10-mm horizontal fracture is carved in the middle of the left boundary. The boundary conditions are: the bottom boundary is fixed, the top boundary is displaced horizontally, and the two lateral boundaries are fixed vertically. We neglect gravity.

The material properties are: shear modulus $G = 10$ MPa, Poisson's ratio $\nu = 0.3$, cohesion strength $c = 40$ kPa, peak and residual friction angle $\phi = \phi_r = 15°$, shear fracture energy $\mathcal{G}_c = 30$ J/m^2, and fracture's length-scale $l = 2$ mm. As in the previous works of Palmer and Rice [83] and Fei and Choo [82], we impose the fracture propagation to be horizontal. Following Fei and Choo's simulations [82], we initialize vertical compressive normal stress to 149 kPa, which results in $\tau_p = 80$ kPa and $\tau_r = 40$ kPa. We mesh the domain near the fracture path with a mapped squared mesh of size $l/4 = 0.5$ mm and the remaining domain with a 1-mm free triangular mesh.

The horizontal force–displacement curve is shown in Fig. 3. The agreement of the peak and residual forces provided by our numerical simulation is very satisfactory. Theoretically, the peak load, i.e., the peak shear stress times the width of the specimen, is 40 kN, and the output of our simulation is 40.387 kN. In the same way, the theoretical residual load is 20 kN and the output of our simulation is 19.978 kN. We estimate the fracture energy from the force–displacement curve, the shaded area in Fig. 3. The output of our model provides a fracture energy equal to 14.6914 J, while the theoretical value is 15 J. Therefore, we report a remarkable agreement between our simulations and expected theoretical values. Moreover, we also include in Fig. 3 the numerical result from the well-known continuous shear deformation (CSD) model reported in [82]. The agreement between both models is remarkable, and is a good proof of the proper performance of our proposal.

We analyze the sensitivity of our model to the phase-field length parameter, l. We run several simulations of the direct shear test problem for several values of l, ranging from 1 to 10 mm. Results are depicted in Fig. 4a. The force–displacement curves for the four values of l confirm that the model is virtually insensitive to the phase-field length
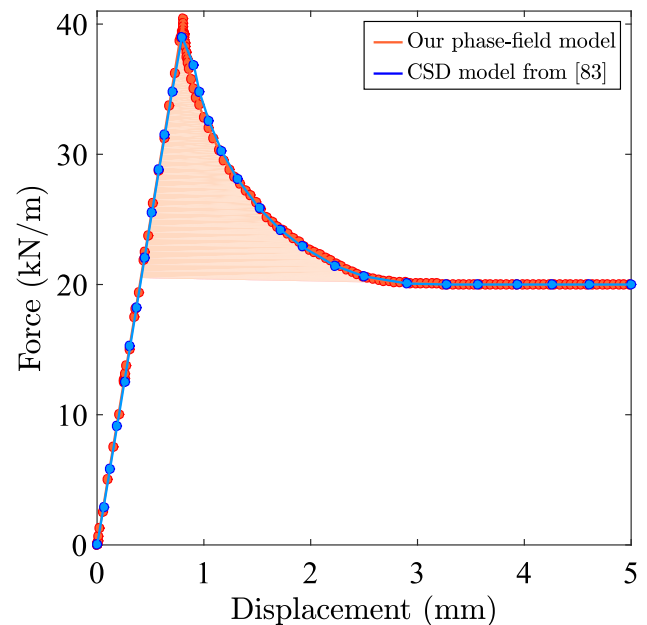

Fig. 3 Horizontal force–displacement curves for the direct shear test. Points are the output of our numerical simulation

parameter. We check the mesh dependency of our model by running three problems of the long-shear apparatus problem. We fix the ratio length scale parameter to mesh size, l/h, to 20 and we run three simulations for three l- and h-values. Results are plot in Fig. 4b. The curves confirm that the model is insensible to the mesh size.

We plot the phase-field distribution at three time steps in Fig. 5. The peak load is given for $U_x = 0.8083$ mm, after this value is reached the phase-field has already emerged and propagate along the whole fracture, Fig. 5a. Afterward, the phase-field value intensifies during the softening stage, Fig. 5b, up to the time the fracture is completely developed, Fig. 5c. At this time, the domain is split into two parts. The upper part slips over the bottom one, and the shear stress between both parts is constant and equal to the residual shear stress, $\tau_r = 40$ kPa, resulting in a theoretical horizontal force of 20 kN.

Fig. 4 Force–displacement curves for the direct shear test with several phase-field length parameters, l, and mesh sizes, h. **a** Here the phase-field length parameter ranges from 1 to 10 mm and the mesh size is set to $h = 0.2$ mm. **b** Here the ratio phase-field length parameter to mesh size is set to 20
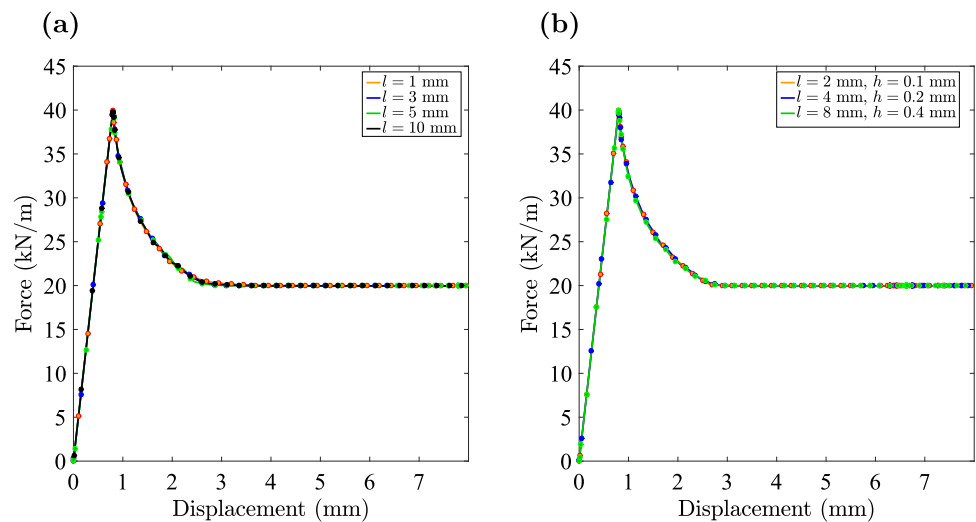

Fig. 5 The evolution of the phase-field variable at three time steps for the direct shear test. The imposed horizontal displacements, U_x, are: **a** 1 mm, **b** 2 mm, and **c** 3 mm

(a) $U_x = 1$ mm

(b) $U_x = 2$ mm

(c) $U_x = 3$ mm

3.2 Biaxial compression test

Our next example is a biaxial compression test. We simulate a laboratory-size specimen under plane strain, different confining pressures and with different residual friction angles. This example allows us to show the ability of the model to simulate the pressure dependence of the peak and residual strengths. We compare our numerical results with peak and residual strengths computed with a mechanical equilibrium model before and after the rupture.

The model setup is shown in Fig. 6a. The domain is 80-mm wide and 170-mm tall rectangular. The bottom boundary is supported by rollers, whereas a prescribed vertical displacement is imposed in the top boundary and zero horizontal displacement in the top middle point. The two lateral boundaries are subjected to the confining pressure, p_c, which is constant during the experiment.

The material properties are: shear modulus $G = 10$ MPa, Poisson's ratio $\nu = 0.3$, cohesion strength $c = 40$ kPa, peak friction angle $\phi = 15°$, shear fracture energy $\mathcal{G}_c = 30$ J/m^2,

Fig. 6 Biaxial compression test.
a The model setup. **b** Vertical
force–displacement curves for
two cases with $p_c = 200$ kPa,
$\phi = 20°$, and $\phi_r = 20°$ and $0°$

(a) Biaxial model

(b) Vertical force-displacement curves
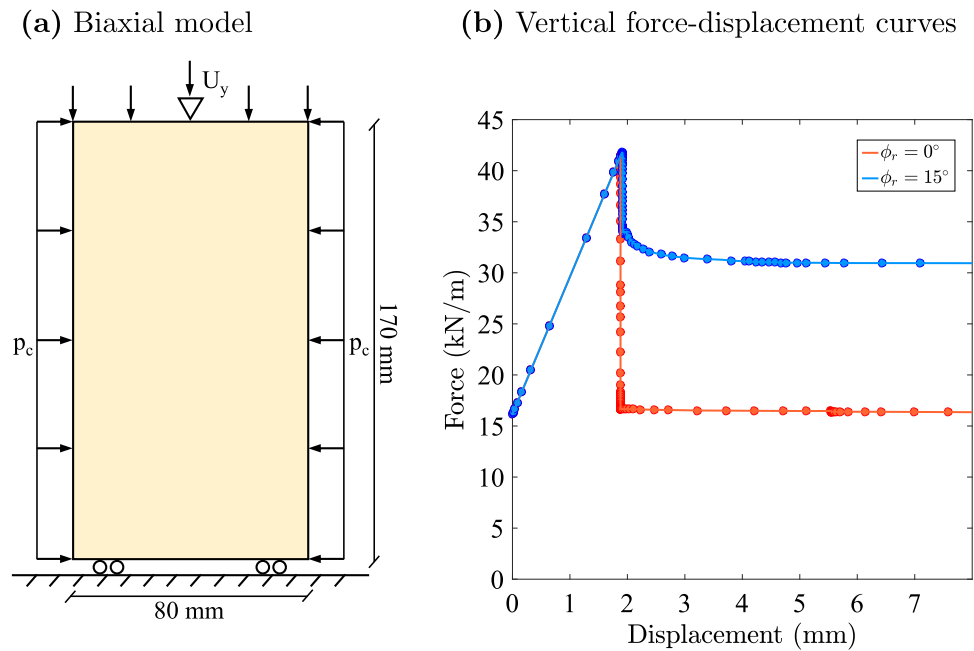
and fracture's length-scale $l = 2$ mm. We neglect gravity. In the center of the domain, we add a small inclusion with a radius of 1 mm and with 20% higher shear modulus to force the fracture nucleation from the center. We simulate three cases of p_c, 50 kPa, 100 kPa, and 200 kPa, and repeat each case with three values of the residual friction angles, $\phi_r = 20°$, $15°$, and $0°$. These simulations let us check whether our model captures the pressure dependence of the peak and residual strengths. We discretize the domain with a free triangular mesh with size $h = 0.2$ mm that satisfy $l/h = 10$.

We include two typical vertical force–displacement curves in Fig. 6b. The confining pressure is $p_c = 200$ kPa, the peak friction angle is $\phi = 20°$, and we consider two residual friction angles, $\phi_r = 20°$ and $0°$. Initially, both vertical forces change linearly with the imposed vertical displacement until the peak strength is reached. The peak strength is the same in both models since they have the same p_c, c, and ϕ. Afterward the fracture propagates suddenly across the domain, reaching both lateral boundaries, and the vertical force suddenly sinks. Our numerical model is able to capture the fracture propagation during the transition from the peak to the residual strengths due to the adaptive time step. Moreover, the curves evidence that the phase-field model is able to simulate the residual strength, which depends on the confining pressure, the residual friction angle, and the fracture path.

We run several simulations of the biaxial compression problem for several values of l, ranging from 1 to 10 mm. The force–displacement curves for the four values of l are included in Fig. 7. As in the previous problem, the curves for the values of l confirm that the model is virtually insensitive to the phase-field length parameter.
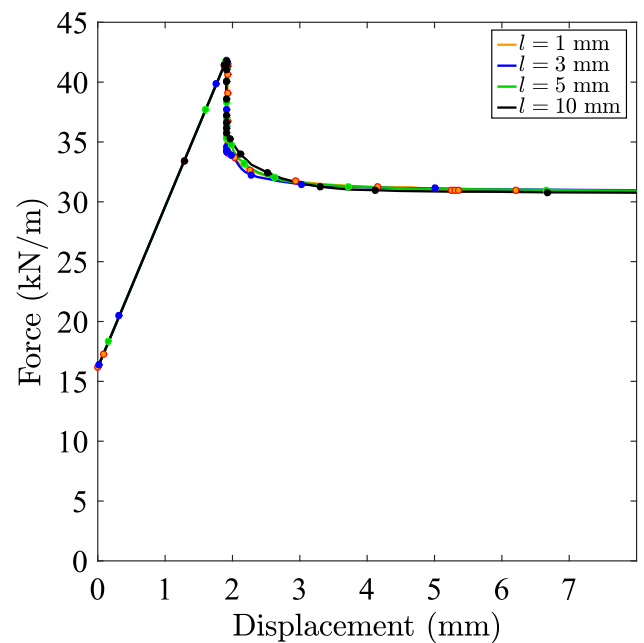

Fig. 7 Force–displacement curves with several phase-field length parameters, l

The evolution of the phase-field variable for $p_c = 200$ kPa, $\phi = 20°$, and $\phi_r = 20°$, at three time steps is shown in Fig. 8. The phase-field is almost zero when the peak strength is reached, Fig. 8a. In fact, due to the isotropic material model and homogeneous stress conditions of the biaxial test, two equally like fracture paths nucleate. This is consistent with the Mohr–Coulomb model. Nevertheless, only of the trajectories evolves and result in the final fracture pattern during the sudden decrease in the peak strength, Fig. 8b.
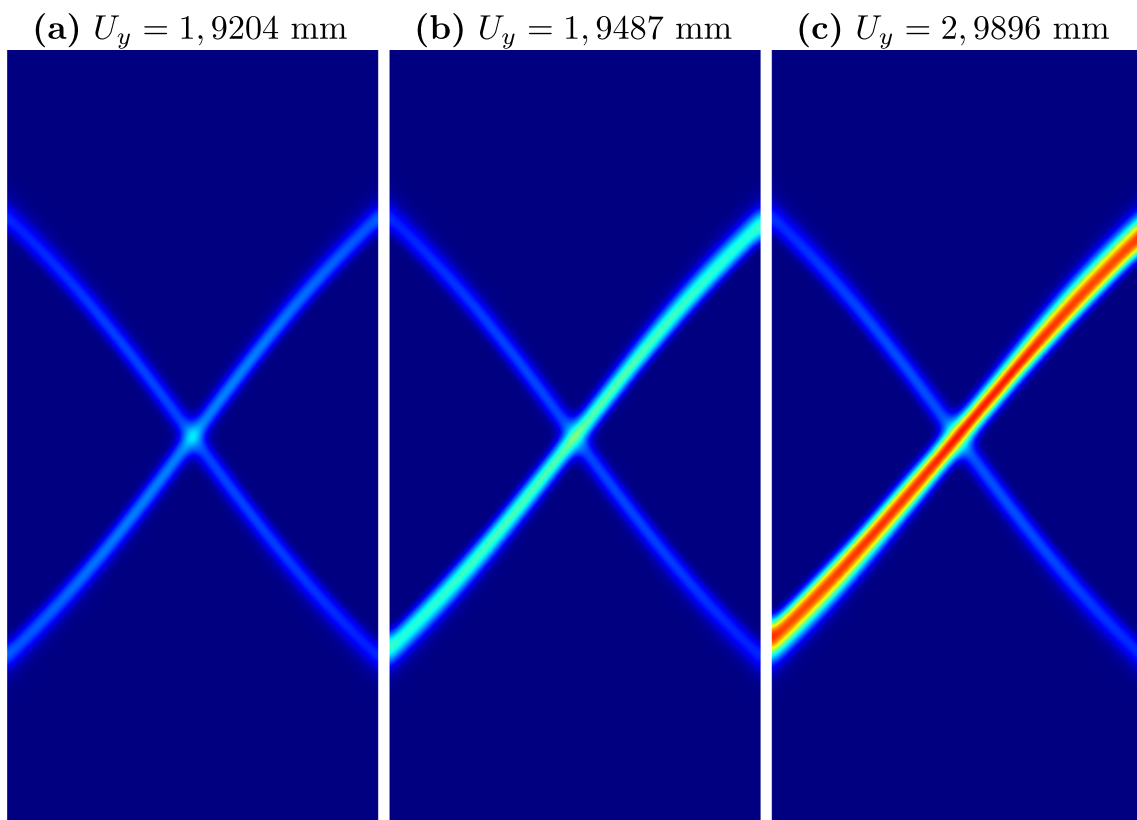
Fig. 8 Biaxial compression test. The evolution of the phase-field variable is plotted at three time steps. The confining pressure is $p_c = 200\,\text{kPa}$, the peak friction angle is $\phi = 20°$, and the residual friction angle $\phi_r = 20°$. The imposed vertical displacements, U_y, are: **a** 1, 9204 mm, **b** 1, 9487 mm, and **c** 2, 9896 mm

Later, the phase-field variable increases its value along the fracture path up to the residual peak strength is reached, Fig. 8c.

We simulate nine cases with several combinations of p_c, ϕ, and ϕ_r values. We also compute the peak and residual strengths applying mechanical equilibrium prior and after the fracture propagation. Given the fracture path, the mechanical equilibrium is illustrated in Fig. 9. The total vertical force applied on the top boundary is F_V, the total horizontal force on the left lateral boundary is F_H, and the tangential and normal forces on the fracture path are T and N respectively. We suppose the nucleation and fracture propagation is instantaneous and the fracture path is a straight line. the angle between the fracture path and the vertical axis is θ. Then, at the onset of the fracture propagation, the tangential force on the fracture is:

$$T = \frac{L}{\sin\theta}c + N\tan\phi, \tag{35}$$

and once the fracture is fully developed, the tangential force on the fracture is:

$$T = N\tan\phi_r. \tag{36}$$

The mechanical equilibrium in the vertical direction is given by:

$$V - T\cos\theta - N\sin\theta = 0, \tag{37}$$

and in the horizontal direction:

$$H + T\sin\theta - N\cos\theta = 0, \tag{38}$$

where H is:

$$H = p_c\frac{L}{\tan\theta}. \tag{39}$$

Solving V from Eq. (37), substituting V in Eq. (38) and operating, the vertical force at the onset of the fracture propagation V_p—peak strength—is:

$$V_p = \frac{1}{\cos\theta - \sin\theta\tan\phi}\left(\frac{L\cdot c}{\sin\theta}\right.$$
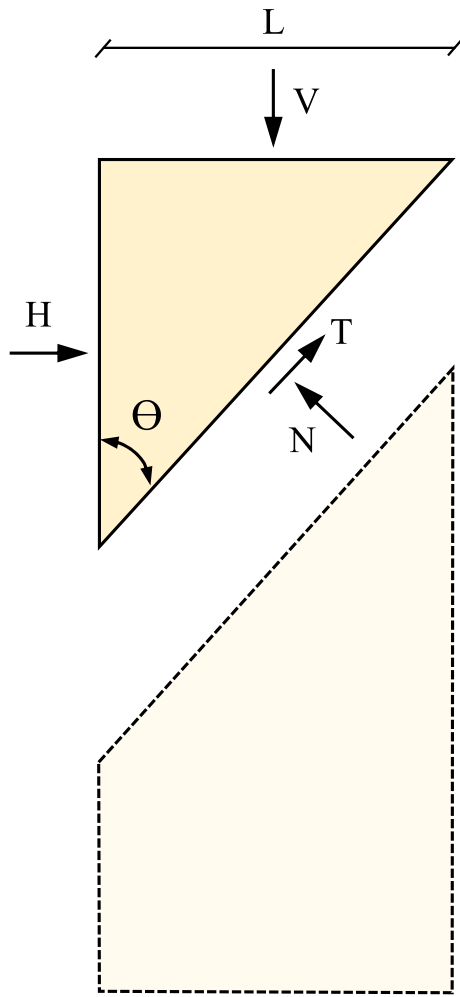$$\left. + p_c\frac{L}{\tan\theta}(\cos\theta tan\phi + \sin\theta)\right), \tag{40}$$

Fig. 9 Triaxial experiment. Mechanical equilibrium

and the vertical force once the fracture is fully propagated V_r—residual strength—is:

$$V_r = \frac{1}{\cos\theta - \sin\theta\tan\phi_r} \left(p_c \frac{L}{\tan\theta} (\cos\theta\tan\phi_r + \sin\theta) \right). \tag{41}$$

We compute V_p and V_r for the nine simulated cases. The results are listed in Table 1. The agreement between both models is remarkable.

3.3 Slope failure analysis

As the last example, we consider the problem of slope failure analysis reported in [33]. Consider the soil slope shown in Fig. 10. The domain is 20 m wide and 10 m tall, with a slope 1:1 on the left side. A 4 m wide rigid footing is placed on the crest of the slope. The slope is first subjected to a body force $b = 20$ kN/m^3, and then these body-force stresses are used as the initial state for the footing loading step. Displacement at the bottom edge is fixed in both directions, while for the right edge, only horizontal displacement is fixed. As the main loading step, a displacement $U_y = 0.3$ m is prescribed in the middle of a rigid foundation, which simulates the effect of a building imposing a stress on the slope.

The elastic parameters of the soil include $E = 10$ MPa and $\nu = 0.4$. The initial friction angle and cohesion are $\phi = 16.7°$ and $c = 40$ kPa, with $\phi_r = 10°$ and $c_r = 0$ kPa as their respective residual values. The phase-field length scale parameter is set to $l = 200$ mm, and the domain is discretized using a free triangular mesh with mesh-size 20 mm. The resulting mesh roughly has 1 M triangles and 500K vertices. The computational time takes about 12 h in our desktop machine with i9-10900 processor with 10 cores and 20 threads.

Due to the relatively high cohesion and low friction angle, the shear-band formation for this problem is particularly interesting. If we plot the evolution of the Mohr–Coulomb's failure envelope right before the onset of fractures, as shown in Fig. 11a, we observe that the failure should onset from both ends of the footing. This fact has also been reported by Haghighat and Pietruszczak [38], however, due to the pre-specification of only one orientation angle (θ), the crack formation from the left side was not captured by Fei and Choo [82]. Therefore, to perform a comparison, we consider two cases:

Table 1 Triaxial experiment

| | $\phi = 15°$ $\phi_r = 15°$ | | | | $\phi = 20°$ $\phi_r = 20°$ | | | | $\phi = 15°$ $\phi_r = 0°$ | | | |
| | Peak stre. | | Residual stren. | | Peak stren. | | Residual stren. | | Peak stren. | | Residual stren. | |
	M. Eq.	Sim	M. Eq.	Sim.	M. Eq.	Sim	M. Eq.	Sim	M. Eq.	Sim	M. Eq.	*Sim*
$p_c = 50$ kPa	15.19	15.15	6.81	7.12	17.30	17.30	8.16	8.24	15.67	15.12	4.00	4.17
$p_c = 100$ kPa	22.00	21.94	13.62	14.27	25.46	25.56	16.32	17.04	22.59	21.93	8.00	8.23
$p_c = 200$ kPa	35.62	34.67	27.23	27.80	41.77	41.48	32.63	33.17	36.45	35.48	16.00	16.30

We list the peak and residual strengths for nine cases in kN. Both strengths are computed with our phase-field model—denoted as Sim.—and using a mechanical equilibrium—denoted as M. Eq.—prior and after the fracture propagation

(a)Slope Failure Model
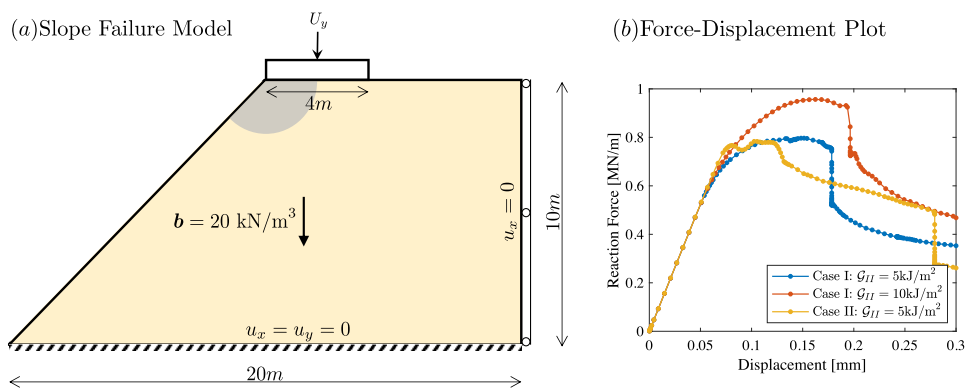
(b)Force-Displacement Plot

Fig. 10 Slope failure analysis. **a** The model setup for the slope failure analysis. The domain is 20 m wide and 10 m tall, with a slope 1:1. A 4 m wide rigid footing is located on the slope's crest, and is subjected to a vertical displacement U_y. The boundary conditions are: bottom edge is fixed in both directions, right edge is fixed horizontally and other faces are traction free. The grey region highlights the damage-inactive (Case I) and damage-active (case II) problems. **b** Force displacement results measured at the point of loading in the middle of the footing. The plots show absolute values

(a)Mohr-Coulomb Failure

$(b)F = 0.7\text{MN/m}$

$(c)F = 0.8\text{MN/m}$

$(d)F = 0.9\text{MN/m}$
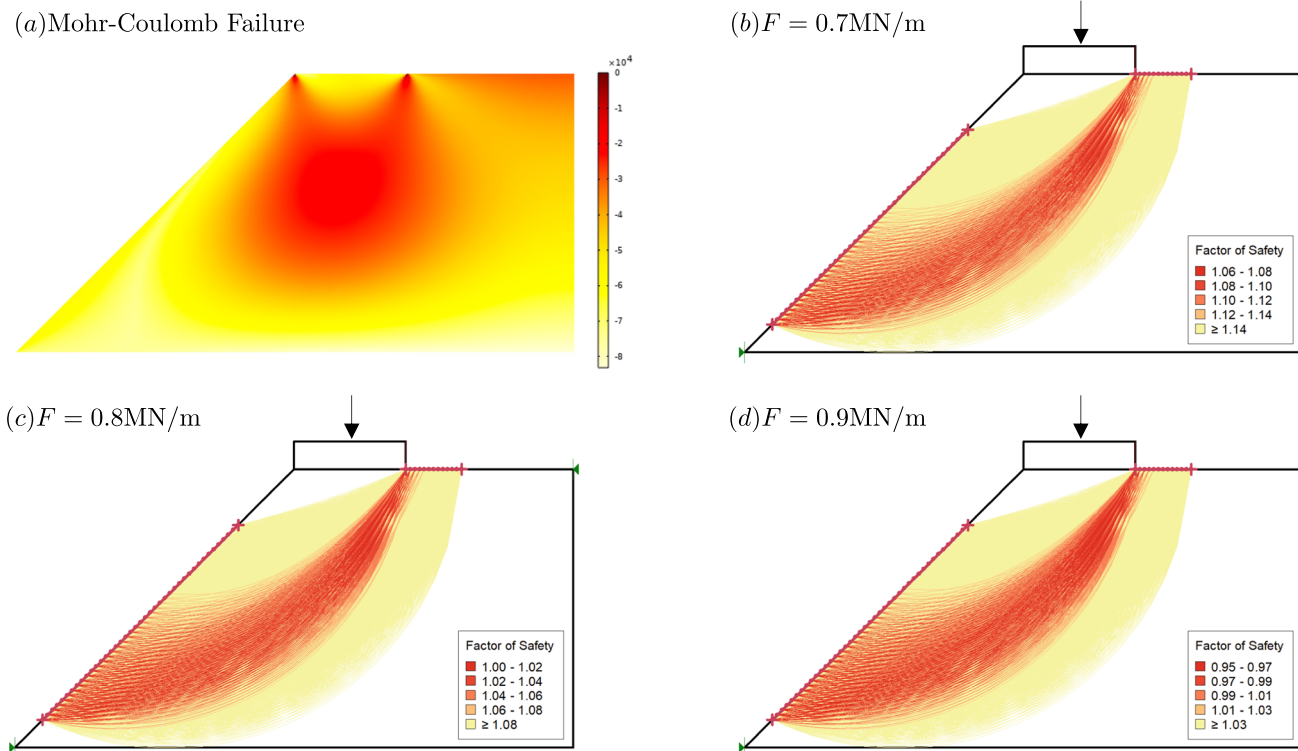
Fig. 11 **a** Mohr–Coulomb failure function plotted right before the onset of localization. The stress around both corners of the footing appear as near-failure critical. **b–d** Mohr–Coulomb's critical surfaces using limit-equilibrium method at different load. $F \approx 0.8\,\text{MN/m}$ is found as the critical load, where factor of safety of the slope reaches 1

I. Shear band formation only from the right corner of the footing by suppressing the phase field variable to zero ($d = 0$) in the gray region (see Fig. 10).

II. Free shear-band formation, which results in two patterns from each side followed by coalesces.

Additionally, we consider two critical fracture energies of $\mathcal{G}_c = 10\,\text{kJ/m}^2$ and $\mathcal{G}_c = 5\,\text{kJ/m}^2$. The final fracture patterns of these two cases are shown in Figs. 12, 13 and 14.

The evolution of phase-field variable for case I, with $\mathcal{G}_c = 5\,\text{kJ/m}^2$, are plotted for different loading steps in Fig. 13. The force–displacement response is plotted in Fig. 10b. As the
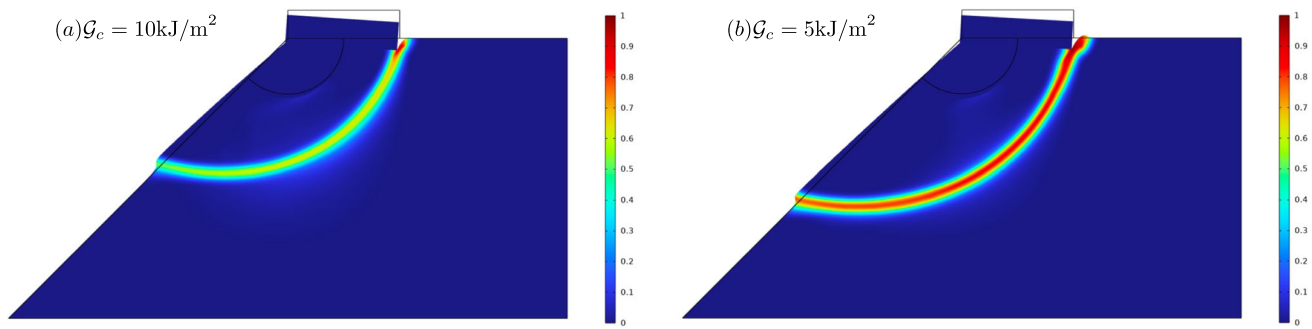
Fig. 12 Damage evolution for the case I slope stability analysis, where the left side is suppressed to have damage development. The plots show the evolution damage at $U_y = 300$ mm for **a** $\mathcal{G}_c = 10$ kJ/m^2 and **b** $\mathcal{G}_c = 5$ kJ/m^2
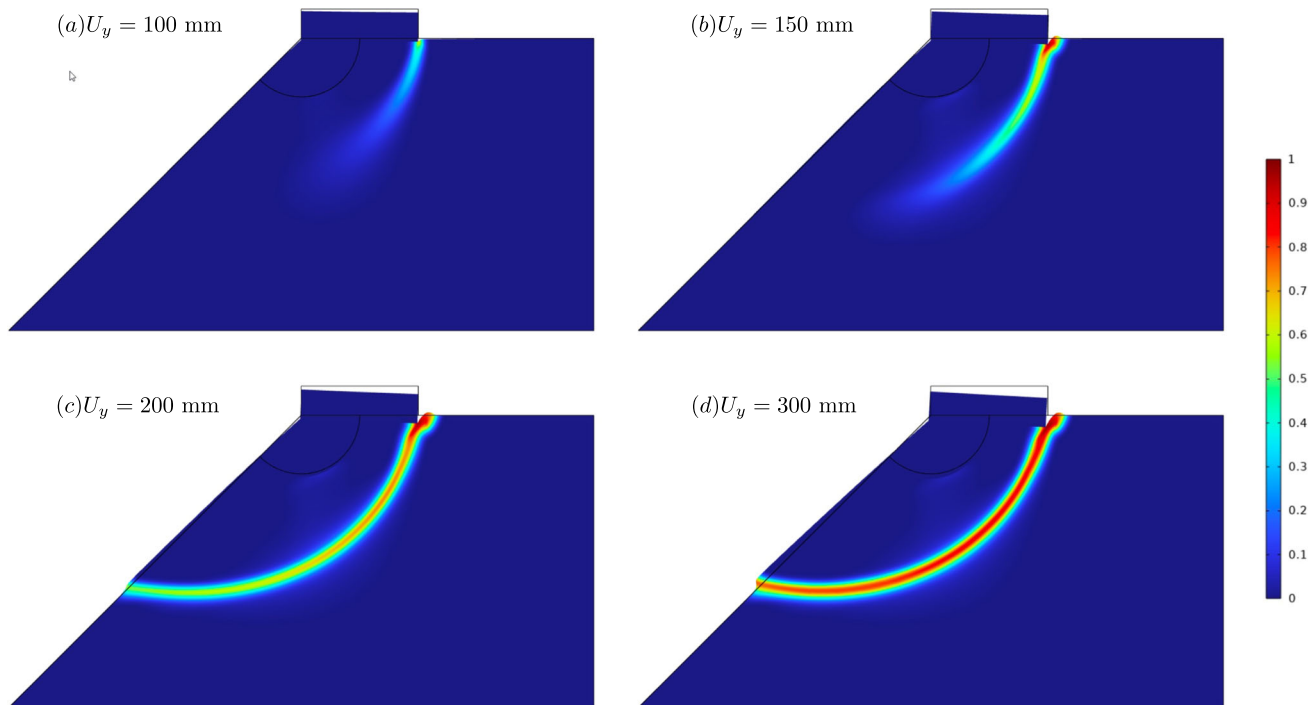

Fig. 13 Damage evolution for the case I slope stability analysis ($\mathcal{G}_c = 5$ kJ/m^2). In this case, the left side is suppressed to develop damage, therefore we have a single crack formation from the footing's right corner. Subplots **a**–**d** show the evolution of the damage parameter at different loading steps

reader can find, the proposed formulation captures the peak and residual loads as well as the crack patterns accurately, and the results are consistent with those reported by Fei and Choo [82]. The failure surface evaluated using phase-field method and the peak-load is well-aligned with potential failure surfaces and critical load $F = 0.8$ MN/m resulting from limit-equilibrium analysis of the slope using the GeoStudio software (see Fig. 11b–d).

Lastly, we run a new set of simulations for case II. The results are plotted in Fig. 14. As we find, here the model captures first a shear band formation from the left corner of the footing. This is in fact expected because of the stress-free surface of the slope creates a more critical failure condition on the left corner. The propagation of the mode, however, stops

because it is directing to Mohr–Coulomb stable regions of the domain. Later, the main failure mode initiates and propagates from the right corner, and collides with the first mode somewhere underneath the footing, which is also consistent with the results of the limit state theories. A final branch is then generated and causes the ultimate failure of the slope. The pick stress, however, does not seem to be very different from those of Case I, as plotted in Fig. 10b.

4 Concluding remarks

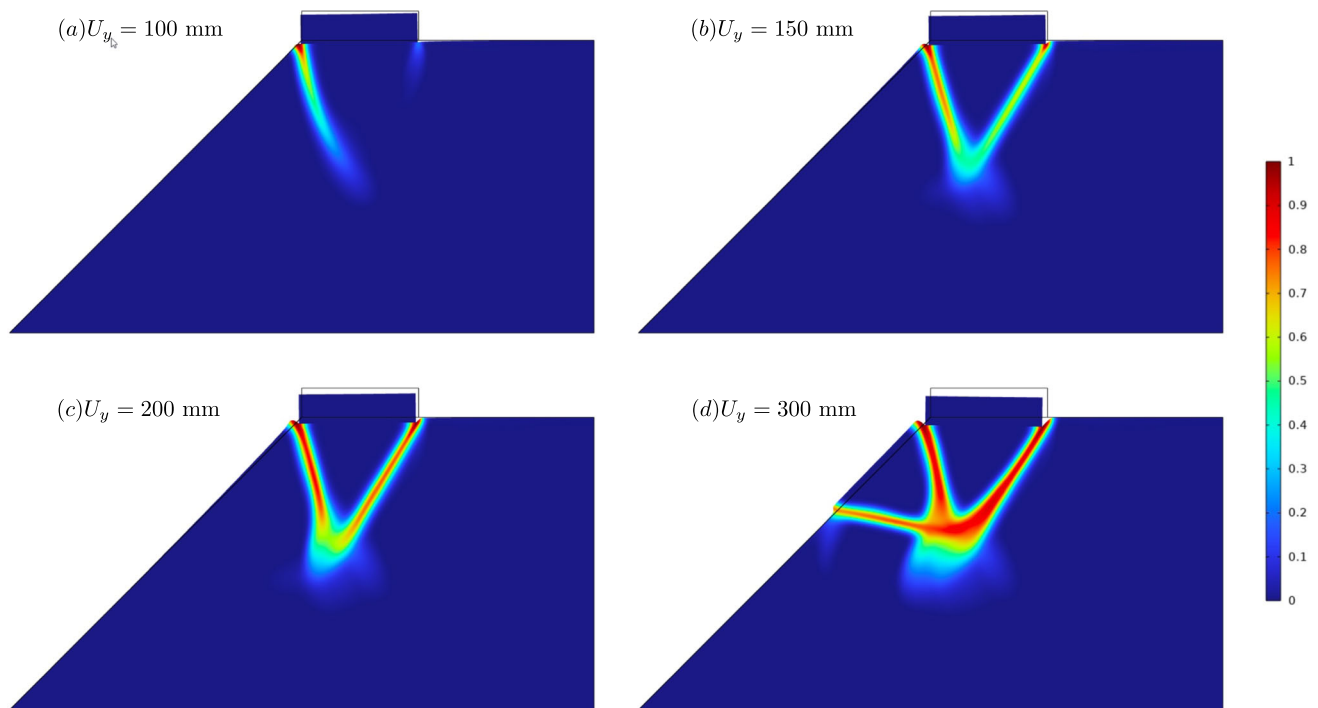We presented a phase-field model of shear fractures using deviatoric stress decomposition (DSD). We validated the

Fig. 14 Damage evolution for the case II slope stability analysis ($\mathcal{G}_c = 5\,\text{kJ/m}^2$). In this case, the damage can initiate from either side and is primarily driven by the crack energy. Subplots **a**–**d** show the evolution of the damage parameter at different loading steps

model by solving reference problems of shear fractures in geotechnical engineering. Our model has excellent performance. The main advantages of our phase-field approach are: (1) the model does not require re-meshing, (2) nucleation, propagation, and fracture path are automatically computed without the need to track fractures or pre-specify orientations, and (3) fracture joining and branching do not need additional algorithms.

For an isotropic Mohr–Coulomb material under homogeneous loading, it has been shown that there are two conjugate surfaces having the same likelihood for shear band formation. In fact, our model captures this for the biaxial compression problem without any intervention. This is the same for the slope stability problem, where our model was able to capture crack initiation from both corners of the foundation. While accurate in peak and residual force calculations, we found that the CSD model of shear fractures is more accurate in capturing such a transition.

The study was limited to modeling two-dimensional problems of compressive fracture. However, the proposed formulation is not limited to any dimensions. Therefore, we plan to explore three-dimensional models as a follow-up study. Additionally, pore-fluid consideration is critically important for modeling failure in geomaterials. This is also an area that will be considered next. Additional paths include incorporating rate-and-state friction models that are best suited for modeling geologic systems, and thermal coupling that is important for modeling geothermal systems.

Data availability statement All data, models, or code generated or used during the study will be made available online at https://github.com/ehsanhaghighat/PhaseField-DSD upon publication.

A Crack driving force for deviatoric stress decomposition

Reminding that $\hat{q}, \tilde{q}_p, \tilde{q}_r$ denote the bulk and fractured deviatoric stresses at peak and residual stages, respectively, and $\hat{q} = 3\mu\varepsilon_q$, with ε_q and the deviatoric strain, the crack driving force during a plastic dissipation process as a result of frictional sliding can be expressed as

$$
\begin{aligned}
\mathcal{H}_{slip} &= \int_{\varepsilon_\gamma^p}^{\varepsilon_\gamma} (\hat{q} - \tilde{q}_r) d\varepsilon_\gamma \\
&= \int_{\varepsilon_\gamma^p}^{\varepsilon_\gamma} (3\mu\varepsilon_q - \tilde{q}_r) d\varepsilon_\gamma \\
&= \frac{1}{6\mu}\left(\hat{q}^2 - \tilde{q}_p^2\right) - \frac{\tilde{q}_r}{3\mu}\left(\hat{q} - \tilde{q}_p\right) \\
&= \frac{1}{6\mu}\left\{(\hat{q} - \tilde{q}_r)^2 - (\tilde{q}_p - \tilde{q}_r)^2\right\}.
\end{aligned}
\tag{42}
$$

Since $q = g(d)\hat{q} + (1 - g(d))\tilde{q}_r$, we will have,

$$
\mathcal{H}_{slip} = \frac{1}{6\mu}\left\{\left(\frac{q - \tilde{q}_r}{g(d)}\right)^2 - (\tilde{q}_p - \tilde{q}_r)^2\right\}.
\tag{43}
$$

We observe that the relations are quite similar to those reported by Fei and Choo [82] using shear stress split, except that shear stresses and strains are replaced now with deviatoric ones and therefore division by 3μ instead of μ.

Noting that total driving energy is expressed as $\mathcal{H} = \mathcal{H}_t + \mathcal{H}_{slip}$, re-arranging Eq. (43), we can write

$$
\mathcal{H} = \left\{\mathcal{H}_t - \frac{1}{6\mu}(\tilde{q}_p - \tilde{q}_r)^2\right\} + \frac{1}{6\mu}\left(\frac{q - \tilde{q}_r}{g(d)}\right)^2.
\tag{44}
$$

Now, one can substitute this relation into the phase field PDE Eq. (9), and with 1D simplifications, integrate the phase field relation, as detailed in [82], to arrive at approximate relations for the evolution of deviatoric stress q as a function damage. Again, since the phase field PDE Eq. (9) and driving force Eq. (44) are very similar to those in [82], all the derivations hold identical and true for the deviatoric stress decomposition. Finally, by imposing length-scale independency to the deviatoric stress evolution, one obtains that

$$
\mathcal{H}_t = \frac{1}{6\mu}(\tilde{q}_p - \tilde{q}_r)^2.
\tag{45}
$$

This completes the derivation of crack driving force relations introduced in Eqs. (30) and (31).

References

1. Rinaldi AP, Rutqvist J, Sonnenthal EL, Cladouhos TT (2015) Coupled THM modeling of hydroshearing stimulation in tight fractured volcanic rock. Transp Porous Media 108:131–150
2. Rinaldi AP, Rutqvist J (2019) Joint opening or hydroshearing? Analyzing a fracture zone stimulation at Fenton Hill. Geothermics 77:83–98
3. Andrés S, Santillán D, Mosquera JC, Cueto-Felgueroso L (2019) Thermo-poroelastic analysis of induced seismicity at the Basel enhanced geothermal system. Sustainability 11:6904
4. Andrés S, Santillán D, Mosquera JC, Cueto-Felgueroso L (2022) Hydraulic stimulation of geothermal reservoirs: numerical simulation of induced seismicity and thermal decline. Water 14:3697
5. Vilarrasa V, Carrera J (2015) Geologic carbon storage is unlikely to trigger large earthquakes and reactivate faults through which CO_2 could leak. Proc Natl Acad Sci 112:5938–5943
6. Juanes R, Hager BH, Herzog HJ (2012) No geologic evidence that seismicity causes fault leakage that would render large-scale carbon capture and storage unsuccessful. Proc Natl Acad Sci 109:E3623–E3623
7. White JA, Foxall W (2016) Assessing induced seismicity risk at CO_2 storage projects: recent progress and remaining challenges. Int J Greenh Gas Control 49:413–424
8. Gupta HK (2002) A review of recent studies of triggered earthquakes by artificial water reservoirs with special emphasis on earthquakes in Koyna, India. Earth Sci Rev 58:279–310
9. McGarr A, Simpson D, Seeber L, Lee W (2002) Case histories of induced and triggered seismicity. In: International handbook of earthquake and engineering seismology, vol 81A. Academic Press LTD, pp. 647–664
10. Rinaldi AP, Improta L, Hainzl S, Catalli F, Urpi L, Wiemer S (2020) Combined approach of poroelastic and earthquake nucleation applied to the reservoir-induced seismic activity in the Val d'Agri area, Italy. J Rock Mech Geotech Eng 12:802–810
11. Pampillón P, Santillán D, Mosquera JC, Cueto-Felgueroso L (2020) Geomechanical constraints on hydro-seismicity: tidal forcing and reservoir operation. Water 12:2724
12. Vilarrasa V, De Simone S, Carrera J, Villaseñor A (2021) Unraveling the causes of the seismicity induced by underground gas storage at Castor, Spain. Geophys Res Lett 48:e2020GL092038
13. Cueto-Felgueroso L, Santillán D, Mosquera JC (2017) Stick-slip dynamics of flow-induced seismicity on rate and state faults. Geophys Res Lett 44:4098–4106
14. Cueto-Felgueroso L, Vila C, Santillán D, Mosquera JC (2018) Numerical modeling of injection-induced earthquakes using laboratory-derived friction laws. Water Resour Res 54:9833–9859
15. Andrés S, Santillán D, Mosquera JC, Cueto-Felgueroso L (2019) Delayed weakening and reactivation of rate-and-state faults driven by pressure changes due to fluid injection. J Geophys Res Solid Earth 124:11917–11937
16. Pampillón P, Santillán D, Mosquera JC, Cueto-Felgueroso L (2023) The role of pore fluids in supershear earthquake ruptures. Sci Rep 13:398
17. Veveakis E, Vardoulakis I, Di Toro G (2007) Thermoporomechanics of creeping landslides: the 1963 Vaiont slide, northern Italy. J Geophys Res Earth Surf 112:1–21
18. Borja RI, Choo J, White JA (2016) Rock moisture dynamics, preferential flow, and the stability of hillside slopes. In: Multi-hazard approaches to civil infrastructure engineering. Springer, pp 443–464
19. González PJ, Tiampo KF, Palano M, Cannavó F, Fernández J (2011) The Lorca earthquake slip distribution controlled by groundwater crustal unloading. Nat Geosci 5(2012):821–825

20. Tiwari DK, Jha B, Kundu B, Gahalaut VK, Vissa NK (2021) Groundwater extraction-induced seismicity around Delhi region, India. Sci Rep 11:1–14

21. Griffith AA (1921) Vi. The phenomena of rupture and flow in solids. Philos Trans R Soc Lond Ser A 221:163–198

22. Irwin GR (1956) Onset of fast crack propagation in high strength steel and aluminum alloys. Technical Report. Naval Research Lab, Washington DC

23. Kachanov L (1958) Rupture time under creep conditions. Izv Akad Nauk SSSR 8:26–31

24. Chan S, Tuba I, Wilson W (1970) On the finite element method in linear fracture mechanics. Eng Fract Mech 2:1–17

25. Rybicki EF, Kanninen MF (1977) A finite element calculation of stress intensity factors by a modified crack closure integral. Eng Fract Mech 9:931–938

26. Bažant ZP, Cedolin L (1979) Blunt crack band propagation in finite element analysis. J Eng Mech Div 105:297–315

27. Pietruszczak S, Mroz Z (1981) Finite element analysis of deformation of strain-softening materials. Int J Numer Methods Eng 17:327–334

28. Simo JC, Ju J (1987) Strain-and stress-based continuum damage models-I. Formulation. Int J Solids Struct 23:821–840

29. Belytschko T, Fish J, Engelmann BE (1988) A finite element with embedded localization zones. Comput Methods Appl Mech Eng 70:59–89

30. Simo JC, Oliver J, Armero F (1993) An analysis of strong discontinuities induced by strain-softening in rate-independent inelastic solids. Comput Mech 12:277–296

31. Simo J, Oliver J (1994) A new approach to the analysis and simulation of strain softening in solids. Fract Damage Quasibrittle Struct, pp 25–39

32. Oliver J (2000) On the discrete constitutive models induced by strong discontinuity kinematics and continuum constitutive equations. Int J Solids Struct 37:7207–7229

33. Regueiro RA, Borja RI (2001) Plane strain finite element analysis of pressure sensitive plasticity with strong discontinuity. Int J Solids Struct 38:3647–3672

34. Wells G, Sluys L (2001) Three-dimensional embedded discontinuity model for brittle fracture. Int J Solids Struct 38:897–913

35. Foster C, Borja R, Regueiro R (2007) Embedded strong discontinuity finite elements for fractured geomaterials with variable friction. Int J Numer Methods Eng 72:549–581

36. Liu F, Borja RI (2008) A contact algorithm for frictional crack propagation with the extended finite element method. Int J Numer Methods Eng 76:1489–1512

37. Dias-da Costa D, Alfaiate J, Sluys L, Júlio E (2009) A discrete strong discontinuity approach. Eng Fract Mech 76:1176–1201

38. Haghighat E, Pietruszczak S (2015) On modeling of discrete propagation of localized damage in cohesive-frictional materials. Int J Numer Anal Methods Geomech 39:1774–1790

39. Moës N, Dolbow J, Belytschko T (1999) A finite element method for crack growth without remeshing. Int J Numer Methods Eng 46:131–150

40. Dolbow J, Moës N, Belytschko T (2001) An extended finite element method for modeling crack growth with frictional contact. Comput Methods Appl Mech Eng 190:6825–6846

41. Moës N, Belytschko T (2002) Extended finite element method for cohesive crack growth. Eng Fract Mech 69:813–833

42. Areias PM, Belytschko T (2005) Analysis of three-dimensional crack initiation and propagation using the extended finite element method. Int J Numer Methods Eng 63:760–788

43. Song J-H, Areias PM, Belytschko T (2006) A method for dynamic crack and shear band propagation with phantom nodes. Int J Numer Methods Eng 67:868–893

44. Borja RI (2008) Assumed enhanced strain and the extended finite element methods: a unification of concepts. Comput Methods Appl Mech Eng 197:2789–2803

45. Sanborn SE, Prévost JH (2011) Frictional slip plane growth by localization detection and the extended finite element method (XFEM). Int J Numer Anal Methods Geomech 35:1278–1298

46. Mikaeili E, Schrefler B (2018) XFEM, strong discontinuities and second-order work in shear band modeling of saturated porous media. Acta Geotech 13:1249–1264

47. Hirmand M, Vahab M, Khoei A (2015) An augmented Lagrangian contact formulation for frictional discontinuities with the extended finite element method. Finite Elem Anal Des 107:28–43

48. Kachanov L (1986) Introduction to continuum damage mechanics, vol 10. Springer, Berlin

49. Bažant ZP, Lin F-B (1988) Nonlocal smeared cracking model for concrete fracture. J Struct Eng 114:2493–2510

50. Leroy Y, Ortiz M (1989) Finite element analysis of strain localization in frictional materials. Int J Numer Anal Methods Geomech 13:53–74

51. Ožbolt J, Bažant ZP (1996) Numerical smeared fracture analysis: nonlocal microcrack interaction approach. Int J Numer Methods Eng 39:635–661

52. Bažant ZP, Jirásek M (2002) Nonlocal integral formulations of plasticity and damage: survey of progress. J Eng Mech 128:1119–1149

53. Silling SA (2000) Reformulation of elasticity theory for discontinuities and long-range forces. J Mech Phys Solids 48:175–209

54. Kilic B, Madenci E (2009) Structural stability and failure analysis using peridynamic theory. Int J Non-Linear Mech 44:845–854

55. Silling SA, Lehoucq RB (2010) Peridynamic theory of solid mechanics. Adv Appl Mech 44:73–168

56. Agwai A, Guven I, Madenci E (2011) Predicting crack propagation with peridynamics: a comparative study. Int J Fract 171:65–78

57. Madenci E, Oterkus E (2014) Peridynamic theory. In: Peridynamic theory and its applications. Springer, pp 19–43

58. Ren H, Zhuang X, Rabczuk T (2016) A new peridynamic formulation with shear deformation for elastic solid. J Micromech Mol Phys 1:1650009

59. Madenci E, Barut A, Futch M (2016) Peridynamic differential operator and its applications. Comput Methods Appl Mech Eng 304:408–451

60. Kamensky D, Behzadinasab M, Foster JT, Bazilevs Y (2019) Peridynamic modeling of frictional contact. J Peridyn Nonlocal Model 1:107–121

61. Song X, Khalili N (2019) A peridynamics model for strain localization analysis of geomaterials. Int J Numer Anal Methods Geomech 43:77–96

62. Zhang H, Zhang X, Liu Y (2022) A peridynamic model for contact problems involving fracture. Eng Fract Mech 267:108436

63. Francfort GA, Marigo J-J (1998) Revisiting brittle fracture as an energy minimization problem. J Mech Phys Solids 46:1319–1342

64. Bourdin B, Francfort GA, Marigo J-J (2000) Numerical experiments in revisited brittle fracture. J Mech Phys Solids 48:797–826

65. Bourdin B, Francfort GA, Marigo J-J (2008) The variational approach to fracture. J Elast 91:5–148

66. Miehe C, Welschinger F, Hofacker M (2010) Thermodynamically consistent phase-field models of fracture: variational principles and multi-field FE implementations. Int J Numer Methods Eng 83:1273–1311

67. Miehe C, Hofacker M, Welschinger F (2010) A phase field model for rate-independent crack propagation: robust algorithmic implementation based on operator splits. Comput Methods Appl Mech Eng 199:2765–2778

68. Kuhn C, Müller R (2010) A continuum phase field model for fracture. Eng Fract Mech 77:3625–3634

69. Borden MJ, Verhoosel CV, Scott MA, Hughes TJ, Landis CM (2012) A phase-field description of dynamic brittle fracture. Comput Methods Appl Mech Eng 217:77–95

70. Verhoosel CV, de Borst R (2013) A phase-field model for cohesive fracture. Int J Numer Methods Eng 96:43–62

71. Borden MJ, Hughes TJ, Landis CM, Verhoosel CV (2014) A higher-order phase-field model for brittle fracture: formulation and analysis within the isogeometric analysis framework. Comput Methods Appl Mech Eng 273:100–118

72. Ambati M, Gerasimov T, De Lorenzis L (2015) Phase-field modeling of ductile fracture. Comput Mech 55:1017–1040

73. Santillán D, Mosquera JC, Cueto-Felgueroso L (2017) Phase-field model for brittle fracture. Validation with experimental results and extension to dam engineering problems. Eng Fract Mech 178:109–125

74. Santillán D, Juanes R, Cueto-Felgueroso L (2017) Phase field model of fluid-driven fracture in elastic media: immersed-fracture formulation and validation with analytical solutions. J Geophys Res Solid Earth 122:2565–2589

75. Santillán D, Juanes R, Cueto-Felgueroso L (2018) Phase field model of hydraulic fracturing in poroelastic media: fracture propagation, arrest, and branching under fluid injection and extraction. J Geophys Res Solid Earth 123:2127–2155

76. Santillán D, Mosquera J-C, Cueto-Felgueroso L (2017) Fluid-driven fracture propagation in heterogeneous media: probability distributions of fracture trajectories. Phys Rev E 96:053002

77. Aldakheel F, Noii N, Wick T, Wriggers P (2021) A global–local approach for hydraulic phase-field fracture in poroelastic media. Comput Math Appl 91:99–121

78. Seles AK, Aldakheel F, Tonkovic Z, Soric J, Wriggers P (2021) A general phase-field model for fatigue failure in brittle and ductile solids. Comput Mech 67:1431–1452

79. Wu J-Y, Nguyen VP, Nguyen CT, Sutula D, Sinaie S, Bordas SP (2020) Phase-field modeling of fracture. Adv Appl Mech 53:1–183

80. Bryant EC, Sun W (2018) A mixed-mode phase field fracture model in anisotropic rocks with consistent kinematics. Comput Methods Appl Mech Eng 342:561–584

81. Zhou S, Zhuang X, Rabczuk T (2019) Phase field modeling of brittle compressive-shear fractures in rock-like materials: a new driving force and a hybrid formulation. Comput Methods Appl Mech Eng 355:729–752

82. Fei F, Choo J (2020) A phase-field model of frictional shear fracture in geologic materials. Comput Methods Appl Mech Eng 369:113265

83. Palmer AC, Rice JR (1973) The growth of slip surfaces in the progressive failure of over-consolidated clay. Proc R Soc Lond A 332:527–548

84. Fei F, Choo J (2021) Double-phase-field formulation for mixed-mode fracture in rocks. Comput Methods Appl Mech Eng 376:113655

85. Kuhn C, Schlüter A, Müller R (2015) On degradation functions in phase field fracture models. Comput Mater Sci 108:374–384

86. Geelen RJ, Liu Y, Hu T, Tupek MR, Dolbow JE (2019) A phase-field formulation for dynamic cohesive fracture. Comput Methods Appl Mech Eng 348:680–711

87. Hughes TJ (2012) The finite element method: linear static and dynamic finite element analysis. Courier Corporation

88. Belytschko T, Liu WK, Moran B, Elkhodary K (2014) Nonlinear finite elements for continua and structures. Wiley, Hoboken

89. Hu T, Guilleminot J, Dolbow JE (2020) A phase-field model of fracture with frictionless contact and random fracture properties: application to thin-film fracture and soil desiccation. Comput Methods Appl Mech Eng 368:113106

90. Lorentz E, Cuvilliez S, Kazymyrenko K (2011) Convergence of a gradient damage model toward a cohesive zone model. C R Mécanique 339:20–26

91. Lorentz E (2017) A nonlocal damage model for plain concrete consistent with cohesive fracture. In J Fract 207:123–159

92. Amor H, Marigo J-J, Maurini C (2009) Regularized formulation of the variational brittle fracture with unilateral contact: numerical experiments. J Mech Phys Solids 57:1209–1229

93. Wu J-Y, Nguyen VP, Zhou H, Huang Y (2020) A variationally consistent phase-field anisotropic damage model for fracture. Comput Methods Appl Mech Eng 358:112629

94. Steinke C, Kaliske M (2019) A phase-field crack model based on directional stress decomposition. Comput Mech 63:1019–1046

95. Strobl M, Seelig T (2016) On constitutive assumptions in phase field approaches to brittle fracture. Procedia Struct Integr 2:3705–3712

96. Strobl M, Seelig T (2015) A novel treatment of crack boundary conditions in phase field models of fracture. PAMM 15:155–156

97. Liu Y, Cheng C, Ziaei-Rad V, Shen Y (2021) A micromechanics-informed phase field model for brittle fracture accounting for unilateral constraint. Eng Fract Mech 241:107358

98. Lancioni G, Royer-Carfagni G (2009) The variational approach to fracture mechanics. A practical application to the French Panthéon in Paris. J Elast 95:1–30

99. Zhang S, Jiang W, Tonks MR (2022) Assessment of four strain energy decomposition methods for phase field fracture models using quasi-static and dynamic benchmark cases. Mater Theory 6:1–24

100. Pietruszczak S (2010) Fundamentals of plasticity in geomechanics. Crc Press, Boca Raton

101. Borja RI (2013) Plasticity, vol 2. Springer, Berlin